



# An immersed boundary method with direct forcing for the simulation of particulate flows

Markus Uhlmann \*

*Departamento de Combustibles Fósiles, CIEMAT, Avenida Complutense 22, 28040 Madrid, Spain*

Received 23 September 2004; received in revised form 19 January 2005; accepted 12 March 2005

Available online 26 May 2005

---

## Abstract

We present an improved method for computing incompressible viscous flow around suspended rigid particles using a fixed and uniform computational grid. The main idea is to incorporate Peskin's regularized delta function approach [Acta Numerica 11 (2002) 1] into a direct formulation of the fluid–solid interaction force in order to allow for a smooth transfer between Eulerian and Lagrangian representations while at the same time avoiding strong restrictions of the time step. This technique was implemented in a finite-difference and fractional-step context. A variety of two- and three-dimensional simulations are presented, ranging from the flow around a single cylinder to the sedimentation of 1000 spherical particles. The accuracy and efficiency of the current method are clearly demonstrated.

© 2005 Elsevier Inc. All rights reserved.

*Keywords:* Immersed-boundary method; Direct interaction force; Finite-difference method; Navier–Stokes equations; Particulate flow; Sedimentation

---

## 1. Introduction

Fluid–particle systems are of considerable scientific and technological interest in a wide range of disciplines. Some examples are: chemical engineering (fluidized beds), medical sciences (blood flow) and civil engineering (sediment transport near river beds). Our present understanding of the dynamics of these systems is far from complete and complex phenomena such as the formation of particle clusters under “turbulent” conditions are still awaiting a definite explanation [1].

In the framework of single-phase turbulent flow the analysis of data from direct numerical simulation (DNS) has proven particularly fruitful [2]. This strategy appears equally promising for the future of multi-phase flows, but the computational challenge is only starting to become accessible. Indeed, in recent

---

\* Tel.: +34 91 3466000; fax: +34 91 3466269.

E-mail address: [markus.uhlmann@ciemat.es](mailto:markus.uhlmann@ciemat.es).

years much effort has been devoted to the design of a feasible method for DNS of the motion of rigid particles immersed in an incompressible fluid [3–9]. By “feasible” it is understood that the method should at the same time: (a) be efficient enough to allow for the treatment of a large number of particles and at sufficiently high values of the relative Reynolds number; (b) provide adequate accuracy in representing the dynamics of the fluid–solid flow.

One way of tackling the computation of suspended particles is to solve the Navier–Stokes equations in the time-dependent fluid domain subject to the no-slip condition at the interfaces with the solid objects. This, however, implies adapting the mesh to the varying positions of the particles during the course of the simulation and leads to a substantial computational cost. An example for such a technique is the arbitrary Lagrangian–Eulerian particle mover of Hu et al. [3] which has been successfully applied to various sedimentation problems.

In order to avoid frequent re-meshing, the flow equations can instead be solved on a fixed grid while the presence of the solid bodies is imposed by means of adequately formulated source terms added to the Navier–Stokes equations. This class of techniques is termed “fictitious domain methods”. One of the precursors, the immersed boundary (IB) method of Peskin, was originally conceived for flows around flexible membranes, specifically the flow in the human heart [10]. The basic idea is to determine a singular force distribution at arbitrary (Lagrangian) positions and to apply it to the flow equations in the fixed reference frame via a regularized Dirac delta function. At the same time, the membrane is moving at the local flow velocity. The additional force term for this problem is simply a function of the deformation of the membrane and of its elastic properties. The careful design of Peskin’s delta function is vital to the efficiency of the method.

The IB method was later extended to Stokes flow around suspended particles [11] and Navier–Stokes flow around fixed cylinders [12]. Höfler and Schwarzer [4] used similar ideas to compute many-particle systems, albeit at relatively low Reynolds numbers. Recently, Feng and Michaelides coupled the IB method with the lattice Boltzmann technique [9]. In references [12,4,9] as well as in related studies [13,14] the singular forces are obtained by means of a feed-back mechanism first proposed by Goldstein et al. [15] and termed “virtual boundary method”. Therein, a deviation from the local desired value of velocity (or position) generates a force in the opposite direction which tends to restore the target value. In other words, a system of virtual springs and dampers is attached to the virtual boundary points, locally forcing a predetermined behavior. An undesirable feature of this indirect formulation of the fluid–solid interaction force is the introduction of additional free parameters. In practice, values for the spring stiffness and damping constant need to be determined in a problem-dependent fashion. Moreover, the characteristic time scales of the oscillations of the spring-damper systems need to be resolved, which can lead to severe restrictions on the time step [12,14].

In order to avoid the drawbacks of the virtual boundary force, Fadlun et al. [16] introduced a direct formulation of the force term. Roughly speaking, the method consists of modifying the entries of the implicit matrix of the discretized momentum equation such that the desired velocity at the boundary points is obtained after each time step. The authors demonstrated that this scheme does not suffer from the time step restrictions of the virtual boundary method. Kim et al. [5] later proposed an explicit variant of the above direct forcing method which allows to maintain the original simple matrix structure of a standard finite-difference method. In both references [16,5] the objective was the efficient computation of flow in complex domains. Although Fadlun et al. [16] present an example of a flow involving moving boundaries, the smoothness of the boundary force during the relative motion was not demonstrated. It was later recognized that the interpolation procedure relating values at fixed grid nodes and values at arbitrarily located boundaries can lead to force oscillations which are undesirable for the purpose of particulate flow simulations [17].

Kajishima and Takiguchi [6] use an extremely simple scheme for modelling the fluid–solid interaction. At the end of a time-step the velocity is explicitly set to the particle’s rigid-body velocity inside each solid

sub-domain. At the interfaces, fluid and solid velocities are smoothly connected by using the solid volume fraction of each computational cell as a weight factor. The method is quite efficient, allowing for the long-time integration of the sedimentation of  $\mathcal{O}(1000)$  particles at a value of 350 for the particle Reynolds number. Although this strategy avoids spurious oscillations of the hydrodynamic force acting on a particle, the force still shows a strong grid dependency [17]. Furthermore, it should be mentioned that the resulting flow-field does not verify the divergence-free condition in the vicinity of the particles.

A different approach was taken by Glowinski et al. [18] who impose rigid-body motion upon the region occupied by the particles by means of a Lagrangian multiplier technique in a finite-element context. In subsequent simulations Glowinski et al. [7] use a first-order accurate, four-step operator splitting scheme for the temporal discretization, including reduced local time steps when updating the particle positions. The method was applied to various sedimentation problems [7] and to the fluidization of  $\mathcal{O}(1000)$  spheres in a narrow gap [19]. It should be kept in mind, however, that the use of a grid system based on tetrahedral elements can break inherent symmetries of the problem. Patankar et al. [20] proposed a related Lagrangian multiplier technique where – instead of velocity – the deformation-rate tensor was imposed in the particle sub-domains, thereby simplifying the treatment of irregularly shaped particles. A further improvement was introduced by Patankar [21] who showed how the need for an iterative procedure could be eliminated when imposing the rigidity constraint. During the review process it was brought to our attention that this scheme has meanwhile been implemented in a control volume context [22] and successfully applied to DNS of particulate flow.

Finally, it should be mentioned that Zhang and Prosperetti [8] have recently proposed a semi-analytic method based upon local Stokesian dynamics in the close vicinity of spherical particles. The matching with the outer (Navier–Stokes) solution is performed iteratively. Up to the present date, however, only computations of two-dimensional sedimentation problems have been reported by these authors.

The objective of the present work is to develop a fictitious domain method in which the forcing term is not obtained by any kind of feed-back mechanism and where oscillations due to the fixed grid are suppressed as much as possible. We will present a strategy to combine the original IB method’s ability to smoothly transfer quantities between Lagrangian and Eulerian positions on the one hand with the advantages of a direct and explicit formulation of the fluid–solid interaction force on the other hand. Thereby, the present method yields less oscillatory particle forces than existing direct methods and a higher efficiency compared to indirect methods.

The organization of the paper is as follows. First, we will briefly state the flow problem in mathematical terms (Section 2) before presenting our technique for imposing the presence of solid bodies upon the fluid in Section 3. The treatment of the equations of motion of the particles is described in Section 4. Results from a number of test problems of increasing complexity as well as an evaluation of the efficiency of our method are presented in Section 5.

## 2. Formulation of the problem

The Navier–Stokes equations for an incompressible fluid read

$$\left. \begin{aligned} \partial_t \mathbf{u} + (\mathbf{u} \cdot \nabla) \mathbf{u} + \nabla p &= \nu \nabla^2 \mathbf{u} + \mathbf{f} \\ \nabla \cdot \mathbf{u} &= 0 \end{aligned} \right\} \mathbf{x} \in \Omega, \quad (1)$$

where  $\mathbf{u}$  is the vector of fluid velocities,  $p$  is the pressure normalized with the fluid density and  $\mathbf{f}$  is a volume force term. These equations are enforced throughout the entire domain  $\Omega$ , comprising the actual fluid domain  $\Omega_f$  and the space occupied by the  $N_p$  suspended solid objects  $\bigcup_{i=1}^{N_p} S_i$  (cf. Fig. 1). In Section 3 the force term  $\mathbf{f}$  will be formulated in such a way as to represent the action of the solids upon the fluid.

In addition to providing appropriate initial conditions and conditions on the outer boundary  $\Gamma$ , we need to describe the motion of the suspended particles under the action of gravity and hydrodynamic forces. This topic will be discussed in Section 4.

### 3. The action of the solids upon the fluid

#### 3.1. Spatial discretization of Eulerian and Lagrangian variables

We employ separate discretizations for the Eulerian and Lagrangian quantities. First, we define a Cartesian, fixed grid  $g_h$  consisting of uniformly distributed nodes  $\mathbf{x}_{ijk} = (i, j, k)h$  covering the domain  $\Omega$  (the constant  $h$  is the mesh width, the integers  $i, j, k$  are the grid indices). A uniform grid is necessary in the present context in order for essential identities of the interpolation scheme to hold (cf. Eqs. (10) and (11)).

Next, let us define for each embedded solid object a number of  $N_L$  points which are evenly distributed over the fluid–solid interface and whose locations are denoted by

$$\mathbf{X}_l^{(i)} \in \partial S_i \quad \forall 1 \leq l \leq N_L, \quad 1 \leq i \leq N_p. \quad (2)$$

We will call these points *Lagrangian force points*. For the sake of simplicity we will henceforth assume that all solid objects are of equal shape and size. Therefore, the number of force points  $N_L$  is the same for each one of them.

The locations  $\mathbf{X}_l^{(i)}$  are used for interpolation purposes and are constant in time with respect to a coordinate system attached to the  $i$ th particle. This concept is related to the *Lagrangian marker points* used in the framework of the IB method [23]. However, in the latter technique the marker points are advected with the local fluid velocity whereas our Lagrangian force points follow the rigid-body motion of the particles and, therefore, do not require additional tracking, i.e. they do not constitute additional degrees of freedom. Furthermore, we associate a discrete volume  $\Delta V_l^{(i)}$  with each force point such that the union of all these volumes forms a thin shell (of thickness equal to one mesh width) around each particle. Similar to references [11,4], this allows us to formulate a volume force at each Lagrangian force point as opposed to the original IB method where a singular force is defined at the Lagrangian marker points. Here we do not apply any forcing to the interior of the particles for reasons of efficiency (cf. related discussion in reference [4]). From two-dimensional test computations of particle sedimentation we could conclude that locating force points throughout the particle volume does not lead to significantly different results [24].

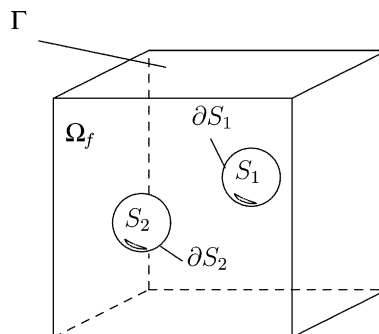


Fig. 1. Example of a configuration with two spherical objects  $S_1, S_2$  and an interstitial fluid domain  $\Omega_f$ . The outer boundary is called  $\Gamma$  and the interfaces between the fluid and the  $i$ th object  $\partial S_i$ .

In [Appendix A](#) the geometrical definitions related to the force point distribution for spherical particles and – in the case of two dimensions – circular objects can be found. Although only these two simple shapes are considered hereafter, the present method equally applies to arbitrarily shaped objects and even to rigid particle surfaces which evolve in time (e.g. due to combustion processes).

### 3.2. Formulation of the volume force

The forcing scheme has the purpose of imposing desired velocity values at selected grid nodes. For a few geometrically simple and stationary solid objects the grid nodes can be located on the interface and forcing reduces to directly modifying the respective matrix entries such that the local velocity vanishes. However, real particles have interfaces with arbitrary, time-dependent locations w.r.t. the grid. Therefore, interpolation steps between Eulerian and Lagrangian positions are necessary.

For the purpose of discussion of the general concepts, let us write the time-discretized momentum equation in the following form:

$$\frac{\mathbf{u}^{n+1} - \mathbf{u}^n}{\Delta t} = \mathbf{rhs}^{n+1/2} + \mathbf{f}^{n+1/2} \quad \forall \mathbf{x} \in \mathcal{g}_h, \quad (3)$$

where  $\mathbf{rhs}^{n+1/2}$  regroups the convective, pressure and viscous terms at some intermediate time level between  $t^n$  and  $t^{n+1}$ . The force term which yields the desired velocity  $\mathbf{u}^{(d)}$  is then simply [16]:

$$\mathbf{f}^{n+1/2} = \frac{\mathbf{u}^{(d)} - \mathbf{u}^n}{\Delta t} - \mathbf{rhs}^{n+1/2} \quad (4)$$

at some selected grid nodes (and zero elsewhere). Kim et al. [5] use grid nodes which are located inside the immersed object and adjacent to its interface, evaluating the desired velocity  $\mathbf{u}^{(d)}$  by means of a linear interpolation procedure. Fadlun et al. [16] discuss several related interpolation techniques. Our personal experience is that in the case of arbitrarily moving objects these procedures can lead to strong oscillations of the hydrodynamical forces due to insufficient smoothing [17].

Instead, we propose to evaluate the force term at the Lagrangian force points  $\mathbf{X}_l^{(i)}$ , viz.

$$\mathbf{F}^{n+1/2} = \frac{\mathbf{U}^{(d)} - \mathbf{U}^n}{\Delta t} - \mathbf{RHS}^{n+1/2} \quad \forall \mathbf{X}_l^{(i)}. \quad (5)$$

In (5) and henceforth we use upper-case letters for quantities evaluated at the locations of the Lagrangian force points  $\mathbf{X}_l^{(i)}$ . The desired velocity at a location on the interface between fluid and solid is simply given by the rigid-body motion of the solid object:

$$\mathbf{U}^{(d)}(\mathbf{X}_l^{(i)}) = \mathbf{u}_c^{(i)} + \boldsymbol{\omega}_c^{(i)} \times (\mathbf{X}_l^{(i)} - \mathbf{x}_c^{(i)}), \quad (6)$$

where  $\mathbf{u}_c^{(i)}$ ,  $\boldsymbol{\omega}_c^{(i)}$ ,  $\mathbf{x}_c^{(i)}$  are the translational and rotational velocity and center coordinates of the  $i$ th solid, respectively.

The two remaining terms on the right-hand side of (5) can be collected as

$$\tilde{\mathbf{U}} = \mathbf{U}^n + \mathbf{RHS}^{n+1/2} \Delta t \quad (7)$$

which corresponds to a preliminary velocity obtained without applying a force term. Its Eulerian counterpart,

$$\tilde{\mathbf{u}} = \mathbf{u}^n + \mathbf{rhs}^{n+1/2} \Delta t \quad \forall \mathbf{x} \in \mathcal{g}_h, \quad (8)$$

is available explicitly in our scheme (cf. Eq. (12a)). In order to complete the evaluation of the forcing term in (3), we still need to provide a mechanism for transferring the preliminary velocity ( $\tilde{\mathbf{u}}$ ,  $\tilde{\mathbf{U}}$ ) and the force itself ( $\mathbf{F}^{n+1/2}$ ,  $\mathbf{f}^{n+1/2}$ ) back and forth between Lagrangian and Eulerian locations.

### 3.3. Transfer of quantities between Lagrangian and Eulerian locations

Here we use the class of regularized delta functions introduced by Peskin [10,23] as kernels in the transfer steps between Lagrangian and Eulerian locations. Dropping the temporal superscripts for convenience, we write:

$$\tilde{\mathbf{U}}(\mathbf{X}_l^{(m)}) = \sum_{\mathbf{x} \in g_h} \tilde{\mathbf{u}}(\mathbf{x}) \delta_h(\mathbf{x} - \mathbf{X}_l^{(m)}) h^3 \quad \forall 1 \leq m \leq N_p; 1 \leq l \leq N_L, \tag{9a}$$

$$\mathbf{f}(\mathbf{x}) = \sum_{m=1}^{N_p} \sum_{l=1}^{N_L} \mathbf{F}(\mathbf{X}_l^{(m)}) \delta_h(\mathbf{x} - \mathbf{X}_l^{(m)}) \Delta V_l^{(m)} \quad \forall \mathbf{x} \in g_h. \tag{9b}$$

The salient properties of the kernels  $\delta_h$  are the following:

- $\delta_h$  is a continuously differentiable function and therefore yields a smoother transfer than e.g. linear interpolation.
- Interpolation using the kernels  $\delta_h$  is second-order accurate for smooth fields (cf. Section 5.1.1).
- The support of the regularized delta function is small, which makes the evaluation of the sums in Eq. (9) relatively cheap. In particular, we use the expression for  $\delta_h$  defined by Roma et al. [25], involving only three grid points in each coordinate direction.
- For all real shifts  $\mathbf{X}$ , we have

$$\sum_{\mathbf{x} \in g_h} \delta_h(\mathbf{x} - \mathbf{X}) h^3 = 1, \tag{10a}$$

$$\sum_{\mathbf{x} \in g_h} (\mathbf{x} - \mathbf{X}) \delta_h(\mathbf{x} - \mathbf{X}) h^3 = 0, \tag{10b}$$

which are discrete analogues of basic properties of the Dirac delta function. As a consequence it can be shown [23] that the total amount of force and torque added to the fluid is not changed by the transfer step in (9b), i.e.

$$\sum_{\mathbf{x} \in g_h} \mathbf{f}(\mathbf{x}) h^3 = \sum_{m=1}^{N_p} \sum_{l=1}^{N_L} \mathbf{F}(\mathbf{X}_l^{(m)}) \Delta V_l^{(m)}, \tag{11a}$$

$$\sum_{\mathbf{x} \in g_h} \mathbf{x} \times \mathbf{f}(\mathbf{x}) h^3 = \sum_{m=1}^{N_p} \sum_{l=1}^{N_L} \mathbf{X}_l^{(m)} \times \mathbf{F}(\mathbf{X}_l^{(m)}) \Delta V_l^{(m)}. \tag{11b}$$

### 3.4. The flow solver

Our Navier–Stokes solver is based upon a conventional fractional-step method for enforcing continuity. A three-step Runge–Kutta scheme is used for the convective terms while the viscous terms are treated by the Crank–Nicholson method, leading to overall formal second-order temporal accuracy.

The spatial derivatives are evaluated by means of second-order, central finite-difference operators on a staggered grid. Staggering implies that each component of velocity  $u_\beta$  is defined at its own Eulerian grid locations, say  $\mathbf{x} \in g_h^{(\beta)}$ . Therefore, the transfer between Eulerian and Lagrangian locations in (9) needs to be carried out for each component individually.

The discretized flow equations, including the fluid–solid coupling term, for the  $k$ th Runge–Kutta step are the following:

$$\tilde{\mathbf{u}} = \mathbf{u}^{k-1} + \Delta t \left( 2\alpha_k v \nabla^2 \mathbf{u}^{k-1} - 2\alpha_k \nabla p^{k-1} - \gamma_k [(\mathbf{u} \cdot \nabla) \mathbf{u}]^{k-1} - \zeta_k [(\mathbf{u} \cdot \nabla) \mathbf{u}]^{k-2} \right), \quad (12a)$$

$$\tilde{U}_\beta(\mathbf{X}_l^{(m)}) = \sum_{\mathbf{x} \in g_h^{(\beta)}} \tilde{u}_\beta(\mathbf{x}) \delta_h(\mathbf{x} - \mathbf{X}_l^{(m)}) h^3 \quad \forall l; m; 1 \leq \beta \leq 3, \quad (12b)$$

$$\mathbf{F}(\mathbf{X}_l^{(m)}) = \frac{\mathbf{U}^{(d)}(\mathbf{X}_l) - \tilde{\mathbf{U}}(\mathbf{X}_l)}{\Delta t} \quad \forall l; m, \quad (12c)$$

$$f_\beta(\mathbf{x}) = \sum_{m=1}^{N_p} \sum_{l=1}^{N_L} F_\beta(\mathbf{X}_l^{(m)}) \delta_h(\mathbf{x} - \mathbf{X}_l^{(m)}) \Delta V_l^{(m)} \quad \forall \mathbf{x} \in g_h^{(\beta)}, 1 \leq \beta \leq 3, \quad (12d)$$

$$\nabla^2 \mathbf{u}^* - \frac{\mathbf{u}^*}{\alpha_k v \Delta t} = -\frac{1}{v \alpha_k} \left( \frac{\tilde{\mathbf{u}}}{\Delta t} + \mathbf{f}^k \right) + \nabla^2 \mathbf{u}^{k-1}, \quad (12e)$$

$$\nabla^2 \phi^k = \frac{\nabla \cdot \mathbf{u}^*}{2\alpha_k \Delta t}, \quad (12f)$$

$$\mathbf{u}^k = \mathbf{u}^* - 2\alpha_k \Delta t \nabla \phi^k, \quad (12g)$$

$$p^k = p^{k-1} + \phi^k - \alpha_k \Delta t v \nabla^2 \phi^k, \quad (12h)$$

where the set of coefficients  $\alpha_k, \gamma_k, \zeta_k$  ( $1 \leq k \leq 3$ ) is given in [26]. The intermediate variable  $\phi$  is the so-called “pseudo-pressure” and has no physical meaning. Eqs. (12e)–(12h) with  $\mathbf{f}$  set to zero correspond to the basic fractional-step method [27].

In the case of periodic boundary conditions, the spatial average of the force term,  $\int_{\Omega} \mathbf{f} \, d\mathbf{x} / \|\Omega\|$ , needs to be subtracted from the momentum equation for compatibility reasons [11,4].

It should be pointed out that the resulting velocity field  $\mathbf{u}^k$  is divergence-free in the sense of the discrete operators. As in previous studies on explicit formulations of the coupling force [16], there are no additional restrictions of the time step stemming from the fluid–solid coupling. This means that stable integration is possible with values of the CFL number close to the theoretical limit of  $\sqrt{3}$  imposed by the basic Runge–Kutta scheme.

In practice, the solution of the Helmholtz (12e) and Poisson (12f) problems is performed as follows. In two space dimensions, a direct solution method based on cyclic reduction [28] is used for solving both types of implicit problems. For reasons of efficient implementation on multi-processor machines in the case of three space dimensions, the Helmholtz problems are simplified by second-order-accurate approximate factorization and the Poisson problem is solved by a multi-grid technique.

#### 4. The motion of the solid particles

The motion of the particles is governed by Newton’s equations for linear and angular momentum of a rigid body. Evaluating the hydrodynamic forces acting upon a particle by means of a momentum balance over the corresponding fluid domain we can write (cf. Appendix B):

$$V_c^{(m)} \left( \rho_p^{(m)} - \rho_f \right) \dot{\mathbf{u}}_c^{(m)} = -\rho_f \underbrace{\sum_l \mathbf{F}(\mathbf{X}_l^{(m)}) \Delta V_l^{(m)}}_{\mathcal{F}^{(m)}} + \left( \rho_p^{(m)} - \rho_f \right) V_c^{(m)} \mathbf{g}, \quad (13a)$$

$$I_c^{(m)} \dot{\boldsymbol{\omega}}_c^{(m)} = -\rho_f \underbrace{\sum_l \left( \mathbf{X}_l^{(m)} - \mathbf{x}_c^{(m)} \right) \times \mathbf{F}(\mathbf{X}_l^{(m)}) \Delta V_l^{(m)}}_{\mathcal{J}^{(m)}} + \rho_f \underbrace{\frac{d}{dt} \int_{S_m} \left( (\mathbf{x} - \mathbf{x}_c^{(m)}) \times \mathbf{u} \right) d\mathbf{x}}_{\mathcal{J}^{(m)}}, \quad (13b)$$

where  $V_c^{(m)}$ ,  $I_c^{(m)}$ ,  $\rho_p^{(m)}$  are the volume, moment of inertia and density of the  $m$ th particle;  $\rho_f$  is the fluid density;  $\mathbf{g}$  is the vector of gravitational acceleration.

The second term on the r.h.s. of (13b) represents the rate of change of angular momentum of the fluid occupying the domain of the  $m$ th solid. Its contribution is due to the fact that applying the fluid–solid coupling force only to the surface of each particle causes a residual non-rigid motion of fluid inside the particle domain  $S_m$ . In practice the integral  $\mathcal{J}^{(m)}$  was evaluated as a sum over each grid cell with the cell’s volumetric solid fraction as a weight. In our three-dimensional applications the rate-of-change term was approximated by supposing rigid-body motion inside the solid volume, i.e. using Eq. (B.4). This was done for reasons of efficiency and a justification is given in Section 5.2.2.

The equations of motion (13) are discretized in time by the same Runge–Kutta procedure as the fluid equations:

$$\frac{\mathbf{u}_c^k - \mathbf{u}_c^{k-1}}{\Delta t} = -\frac{\rho_f}{V_c(\rho_p - \rho_f)} \mathcal{F}^k + 2\alpha_k \mathbf{g}, \quad (14a)$$

$$\frac{\mathbf{x}_c^k - \mathbf{x}_c^{k-1}}{\Delta t} = \alpha_k \left( \mathbf{u}_c^k + \mathbf{u}_c^{k-1} \right), \quad (14b)$$

$$\frac{\boldsymbol{\omega}_c^k - \boldsymbol{\omega}_c^{k-1}}{\Delta t} = -\frac{\rho_f}{I_c} \mathcal{J}^k + \frac{\rho_f}{I_c} \frac{(\mathcal{J}^k - \mathcal{J}^{k-1})}{\Delta t}, \quad (14c)$$

where we have dropped the superscript for the particle index  $^{(m)}$  in favor of the Runge–Kutta sub-step index. Also note that the angular position is not needed for advancing the equations. In the case of evaluating the rate-of-change term from a full rigidity approximation, Eq. (14c) is replaced by

$$\frac{\boldsymbol{\omega}_c^k - \boldsymbol{\omega}_c^{k-1}}{\Delta t} = -\frac{\rho_f}{\rho_p - \rho_f} \frac{1}{(I_c/\rho_p)} \mathcal{J}^k. \quad (15)$$

#### 4.1. Weak coupling of fluid and particle equations

Our scheme consists in first solving the fluid equations (12) with the particle positions and velocities known from the previous Runge–Kutta level and then solving the particle equations (14) as indicated, using the most recent flow field. In order to simplify the notation, consider the following model system where each sub-system contains only one variable, flow velocity  $\mathbf{u}$  and particle center velocity  $\mathbf{u}_c$ , respectively:

$$\mathbf{u}^k = \mathbf{u}^{k-1} + \Psi_1(\mathbf{u}^k, \mathbf{u}^{k-1}, \mathbf{u}^{k-2}, \mathbf{u}_c^{k-1}), \quad (16a)$$

$$\mathbf{u}_c^k = \mathbf{u}_c^{k-1} + \Psi_2(\mathbf{u}_c^{k-1}, \mathbf{u}^{k-1}, \mathbf{u}^{k-2}), \quad (16b)$$

and the functions  $\Psi_1$ ,  $\Psi_2$  represent the time advancement of each sub-system. This model is representative of our full system inasmuch as it is implicit in the former case and explicit in the latter. The coupling between both sub-systems is explicit, also called “weak coupling”.



It has been noted in the past that the treatment of very light particles presents a problem for methods where the fluid equations are weakly coupled to the equations of motion for the rigid particles. Hu et al. [3] show how growing oscillations of the particle velocity can arise depending on the added mass in the case of a particle accelerating from rest due to gravity while using fully explicit coupling. In practice we have found that there is a lower limit of the density ratio for stable weakly coupled integration of the fluid–particle system for the present method:  $\rho_p/\rho_f \gtrsim 1.05$  for circular disks,  $\rho_p/\rho_f \gtrsim 1.2$  for spherical particles. We have observed that the limiting value does not depend significantly upon the chosen time step. Incidentally, the explicitly coupled scheme of Kajishima and Takiguchi [6] allows for density ratios  $\rho_p/\rho_f \gtrsim 2$  (circular disks) according to our experience.

In cases where the weakly coupled procedure is unstable, Gauss–Seidel-like sub-iterations for each Runge–Kutta step can be performed [24]. In order to avoid the additional overhead associated with iterative coupling, fully implicit coupling – like the method proposed in reference [21] – is in principle preferable. This aspect is left as a future extension of our scheme. In the following examples we have chosen density ratios above the indicated threshold.

## 5. Results

### 5.1. Test cases with one-way coupling

First we consider configurations where the equations for the motion of particles (14) need not be solved because Lagrangian velocity and position data are explicitly known. Thereby, the principle features of our new force formulation can be validated in a separate way. Furthermore, we will initially focus on two-dimensional flows for simplicity.

#### 5.1.1. Taylor–Green vortices

In order to establish the influence of the relative position of the immersed boundary with respect to the fixed grid, we consider the case of an array of decaying vortices with analytical solution

$$u(x, y, t) = \sin(k_x x) \cos(k_y y) e^{-(k_x^2 + k_y^2)vt}, \quad (17a)$$

$$v(x, y, t) = -\frac{k_x}{k_y} \sin(k_y y) \cos(k_x x) e^{-(k_x^2 + k_y^2)vt}, \quad (17b)$$

$$p(x, y, t) = \frac{1}{2} \left( \cos^2(k_y y) \frac{k_x^2}{k_y^2} - \sin^2(k_x x) \right) e^{-2(k_x^2 + k_y^2)vt}, \quad (17c)$$

where  $k_x = k_y = \pi$ . This case is simulated in an embedded circular domain with radius unity and centered at the origin of the computational domain  $\Omega = [-1.5, 1.5] \times [-1.5, 1.5]$ . This flow has been computed in reference [5] in a quadrilateral embedded domain. The viscosity is set to  $\nu = 0.2$  and the equations are advanced for  $0 \leq t \leq 0.3$  using a time step of  $\Delta t = 0.001$ . The exact solution (17) provides: (a) the initial field at  $t = 0$ ; (b) the time-dependent boundary conditions at the domain boundary  $\Gamma$ ; (c) the time-dependent desired velocity values  $\mathbf{U}^{(d)}$  at the circumference of the embedded circle.

Fig. 2 shows the maximum error of velocity for grid nodes located inside the embedded domain, plotted as a function of the mesh size  $h$ . Second order convergence is observed, which confirms the accuracy of the interpolation with the regularized delta function in the case of smooth fields. The important result of this case is that the error is not very sensitive to the position of the immersed boundary relative to the grid. This feature can be demonstrated by fixing the resolution ( $h = 0.05$ ) and shifting the circular sub-domain

horizontally by fractions of the mesh-width. Fig. 3 shows that the error varies indeed very smoothly as a function of the shift.

### 5.1.2. A cylinder in uniform cross-flow

We place a cylinder with radius  $r_c = 0.15$  at the origin of the domain  $\Omega_1 = [-1.85, 6.15] \times [-4, 4]$ . At the three boundary segments  $x = -1.85$ ,  $y = -4$  and  $y = 4$  we impose a uniform free-stream velocity  $\mathbf{u} = (1, 0)$ . The boundary at  $x = 6.85$  is treated by a convective outflow condition. A homogeneous Neumann condition is used at all four boundaries for the Poisson equation of pseudo-pressure (12f).

The uniform grid has  $1024 \times 1024$  nodes, i.e. the ratio of particle diameter to mesh size is  $D/h = 38.4$ . This corresponds to the finest grid used in reference [12]. The Reynolds number  $Re_D = \frac{u_\infty D}{\nu}$  is set to 100. The time step is  $\Delta t = 0.003$ , leading to a maximum CFL number of approximately 0.6.

Table 1 shows the resulting drag and lift coefficients  $C_D$ ,  $C_L$  as well as the Strouhal number  $St$  defined from the oscillation frequency of the lift force. It should be mentioned that drag and lift forces were evaluated as sums over the fluid–solid coupling terms (12c) and summing contributions from the three Runge–Kutta sub-steps (cf. [5] and the discussion on methods for determining drag/lift forces in [12]). The agreement with reference values from the literature [29] is generally good. In particular, the Strouhal number is predicted within 4% error, the amplitude of the lift and drag fluctuations with errors of 3% and 8%, respectively. However, the mean drag is overpredicted by 11%; this is also true for the following case of an oscillating cylinder where an overprediction of approximately 10% is obtained (cf. Table 2). Using the IB method, Lai and Peskin [12] obtained a similar overprediction of the mean drag in this case and attributed the discrepancy to the confinement effect due to the finite distance of the lateral boundaries which are treated as slip walls. The importance of the domain size was previously demonstrated by Behr et al. [30]. More recently, Linnick and Fasel [31] reported an irregular drag coefficient for a computational domain measuring approximately  $18D$  in the cross-stream direction; using  $43D$  corrected the problem in their case. For the purpose of verification, we have repeated our simulation in a larger domain  $\Omega_2 = 1.5\Omega_1$  (i.e.  $40D \times 40D$ ) while maintaining the same spatial resolution ( $1536 \times 1536$  nodes) and time step. As can be seen in Table 1 the effect is a decrease of the mean drag, leading to a reduced error of less than 8%. Furthermore, the amplitude of the lift fluctuations now matches with the reference values from [29] and the prediction of the Strouhal number is further improved.

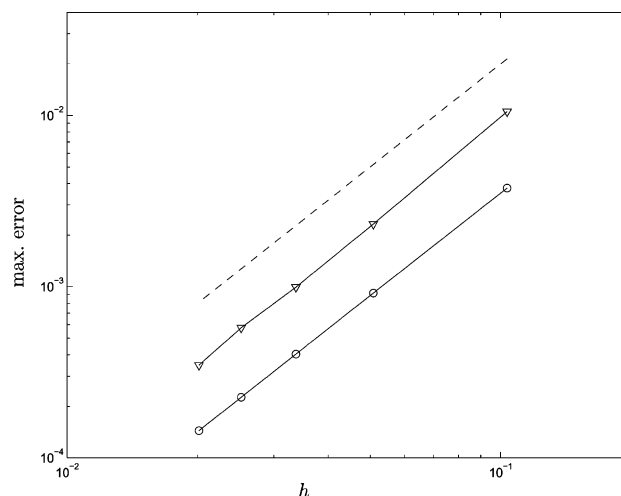


Fig. 2. Maximum error of the velocity field in the case of Taylor–Green vortices. The error is shown as a function of the mesh width  $h$  without embedded boundary (○) and with circular embedded boundary (Δ); the dashed line is proportional to  $h^2$ .

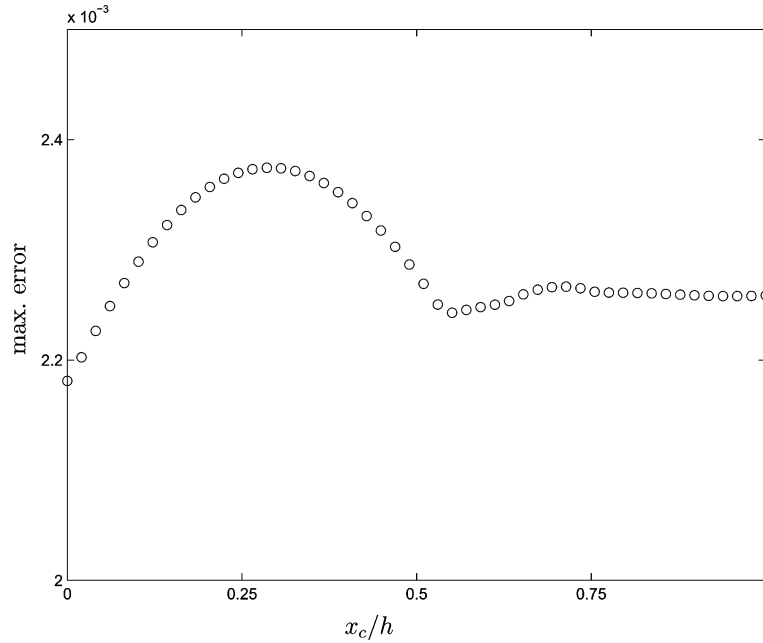


Fig. 3. Maximum error of the velocity field in the case of Taylor–Green vortices. The error is shown as a function of the horizontal position of the embedded circle, for fixed  $h = 0.05$ .

Table 1

Dimensionless coefficients obtained from the simulation of the flow around a stationary cylinder at  $Re_D = 100$ , using  $D/h = 38.4$ ,  $\Delta t = 0.003$

	$\bar{C}_D$	$C'_D$	$C'_L$	$St$
Present	1.501	$\pm 0.011$	$\pm 0.349$	0.172
Present, enlarged domain $\Omega_2$	1.453	$\pm 0.011$	$\pm 0.339$	0.169
Liu et al. [29]	1.350	$\pm 0.012$	$\pm 0.339$	0.165

The enlarged domain  $\Omega_2$  measures  $40D \times 40D$ .

Fig. 4 shows the time-averaged pressure coefficient  $C_p = (p - p_\infty)/u_\infty^2$  along the cylinder surface. The data are plotted at the nearest pressure nodes outside the cylinder. A very good agreement with the well-established results of Park et al. [32] is obtained, including the stagnation and base region.

We now set the cylinder in time-periodic motion in the direction which is perpendicular to the cross-flow, i.e.:

$$y_c(t) = A \sin(2\pi f_f t), \quad (18)$$

with the amplitude set to  $A = 0.2D$  and the frequency  $f_f$  to 0.8 times the natural shedding frequency, i.e.  $f_f = 0.52$ . The maximum velocity of the cylinder motion is approximately  $0.2u_\infty$ . The value for the Reynolds number is set to  $Re_D = 185$  in order to match the conditions of reference [33]. All other parameters remain the same as in the corresponding stationary case above. In particular, the smaller domain  $\Omega_1$  was used if not otherwise stated.

Fig. 5 shows the periodic variation of the drag coefficient as a function of the cylinder’s position. The important observation here is that the curve is reasonably smooth, which demonstrates our present scheme’s ability to handle arbitrary motion w.r.t. the fixed grid. Using the regularized delta function of Peskin [23] with wider support of 4 grid points reduces the remaining mild oscillations even further (Fig. 5). However, in the latter case the cost of evaluating the interpolation sums is significantly higher (more than twice in three dimensions). For the purpose of comparison we have included in Fig. 5 the corresponding result obtained by means of the forcing method of Kajishima and Takiguchi [6], implemented into the present solver as described in detail in [17]. Strong oscillations on the scale of the mesh-width are evident, indicating that the solid-volume-fraction-weighting used therein is a less efficient smoothing mechanism. It can be seen from Table 2 that the present method yields a higher drag than our computations using the method of reference [6]; the use of the 4-point delta function increases the mean drag even further. It should be noted that the smoothing scheme proposed by Kajishima and Takiguchi [6] corresponds to the most compact stencil among the three methods discussed here (solid-volume-fraction-weighting, 3-point delta function, 4-point delta function). Consequently, our results indicate that the smoother the representation of the interface, the higher the value of the mean drag. Finally, as in the case of the stationary cylinder, it was verified that our over-prediction of the drag diminishes with the domain size: the error of  $\bar{C}_D$  decreases to approximately 8% for domain  $\Omega_2$  (Table 2). The predicted value for the r.m.s. lift coefficient also diminishes with the domain size, yielding an error of 8% with respect to reference [33] for  $\Omega_2$ .

## 5.2. Sedimentation of circular discs

The following two cases treat the sedimentation of circular discs in an ambient container. At  $t = 0$  all particles are at rest. The initial velocity field is  $\mathbf{u}(t = 0) = 0 \forall \mathbf{x} \in \Omega$  and no-slip conditions apply at the boundaries,  $\mathbf{u} = 0 \forall x \in \Gamma$ . Homogeneous Neumann boundary conditions are used for the pseudo-pressure. The particle Reynolds number is defined from the particle velocity,  $Re_D = |\mathbf{u}_c|D/\nu$ .

### 5.2.1. Drafting–kissing–tumbling case

Two particles with identical density and radius are accelerating from rest due to the action of gravity. Initially, they have the same horizontal position, but some vertical offset. The trailing particle catches up with the leading one due to the reduced drag in the former particle’s wake. This case has frequently been considered in the literature [3,7–9]. At a later stage the present case involves direct particle–particle interaction, i.e. the particles approach each other closely, albeit probably not closely enough for collision/film

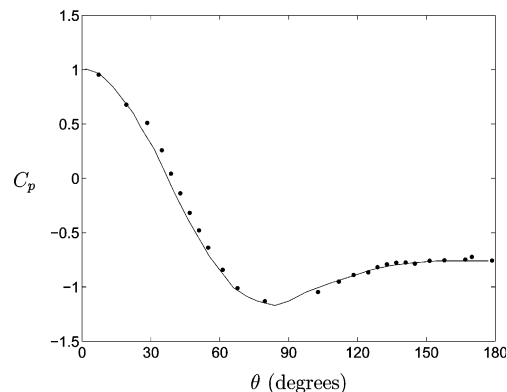


Fig. 4. Surface pressure coefficient  $C_p$  as a function of the angle  $\theta$  ( $\theta = 0^\circ$  corresponds to the stagnation point,  $\theta = 180^\circ$  to the base point) for the case of a stationary cylinder in uniform flow at  $Re_D = 100$ . •, present results; —, data from Park et al. [32].

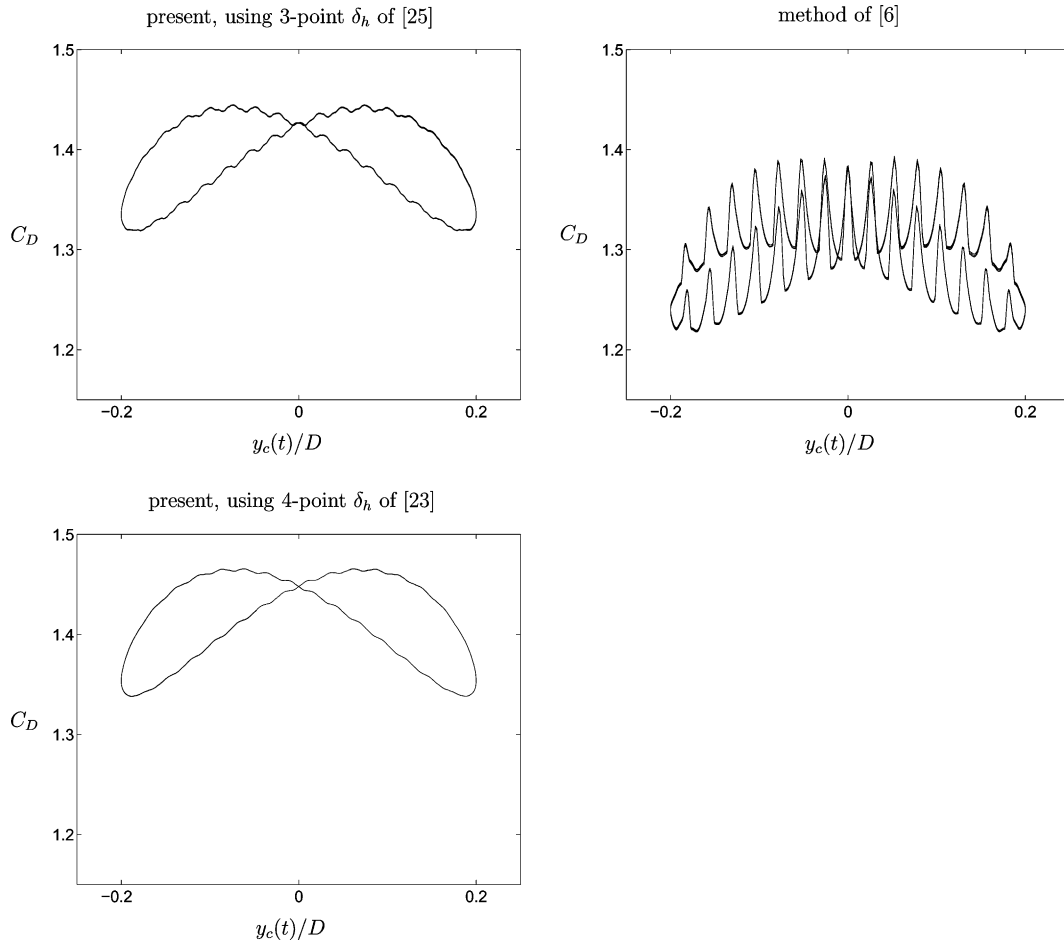


Fig. 5. Time-periodic variation of the drag coefficient in the case of a translationally oscillating cylinder in uniform cross-flow at  $Re_D = 185$  with  $D/h = 38.4$  and  $CFL \approx 0.6$ . Left column: present method, using two regularized delta functions with different support. Right graph: method of Kajishima and Takiguchi [6], implemented into the present solver as described in [17].

rupture to take place. However, very thin liquid inter-particle films cannot be resolved by a typical grid and therefore the correct build-up of repulsive pressure is not captured which in turn can lead to possible partial “overlap” of the particle positions in the numerical computation. In practice, various authors use artificial

Table 2

Dimensionless coefficients obtained from the simulation of the flow around a cylinder at  $Re_D = 185$  which oscillates near the natural shedding frequency and using  $D/h = 38.4$  and  $\Delta t = 0.003$

	$\bar{C}_D$	$C'_D$	$(C_L)_{rms}$
Present	1.380	$\pm 0.063$	0.176
Present, enlarged domain $\Omega_2$	1.354	$\pm 0.065$	0.166
Present, 4-point $\delta_h$ of [23]	1.402	$\pm 0.064$	0.172
Kajishima and Takiguchi's scheme [6]	1.282	$\pm 0.088$	0.223
Lu and Dalton [33]	1.25		0.18

The domain  $\Omega_1$  has been used, except where otherwise stated.

repulsion potentials which prevent such non-physical situations [4,3,7]. In order to allow for comparison with available data, we apply the collision strategy of Glowinski et al. [18], relying upon a short-range repulsion force (stiffness  $\varepsilon_p = 5 \times 10^{-7}$  and force range  $\rho = 3h$ , in the terminology of reference [18]).

This case corresponds to the one computed in [7, Section 8.4]. The physical parameters of the problem are the following:

- domain size  $\Omega = [0, 6] \times [-1, 1]$ ;
- disc radius  $r_c^{(1)} = r_c^{(2)} = 0.125$ ;
- initial location of the discs  $\mathbf{x}_c^{(1)}(t=0) = (1, +0.001)$ ,  $\mathbf{x}_c^{(2)}(t=0) = (1.5, -0.001)$ ;
- density ratio  $\rho_p^{(1)}/\rho_f = \rho_p^{(2)}/\rho_f = 1.5$ ;
- fluid viscosity  $\nu = 0.01$ ;
- gravitational acceleration  $\mathbf{g} = (981, 0)$ .

This leads to maximum values for the particle Reynolds number of approximately 480 and 430, respectively. The numerical parameters were:

- mesh width  $h = 1/256$ , i.e.  $D/h = 64$ ;
- time step  $\Delta t = 0.0001$ , which leads to a maximum *CFL* number around 0.85.

Figs. 6–8 show our present results as well as the ones kindly re-computed and provided by T. Pan (private communication) using the method of reference [7]. The latter results are, therefore, not exactly equivalent to those presented in [7]. As marked in the figures, the artificial repulsion force is non-zero during the following interval:  $0.1687 \leq t \leq 0.2582$ .

For the vertical position and velocity, we observe a very close agreement between both results – up to the time of direct particle interaction (“kissing”). During the “tumbling” stage, which is the manifestation of a strong instability, we cannot expect more than a qualitative accord among simulations performed with quite different numerical methods. It is noteworthy that the leading and trailing particle reverse their roles (i.e. the vertical position curves cross-over) in both results, albeit at different times. The results for the horizontal position and velocity, on the other hand, differ considerably during the “drafting” stage.

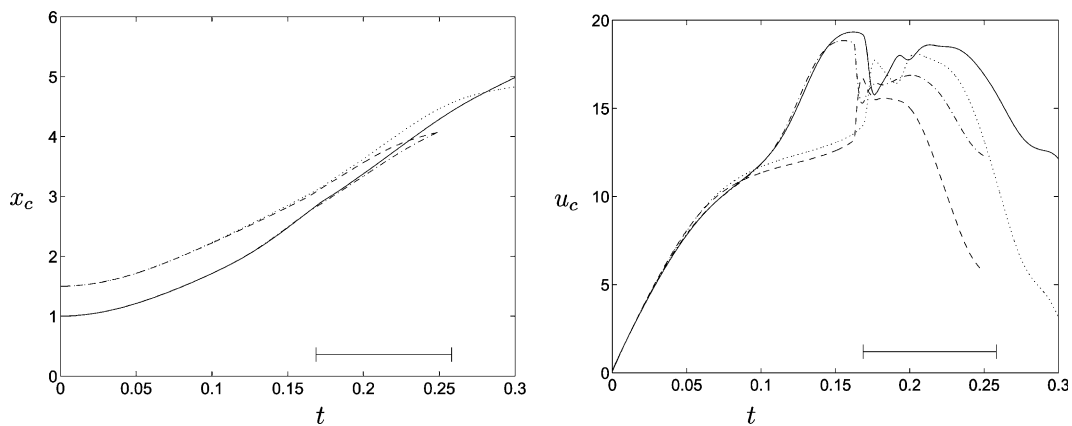


Fig. 6. Drafting–kissing–tumbling of two sedimenting discs with density  $\rho_p/\rho_f = 1.5$  which are initially aligned vertically. Results obtained with the present method,  $\Delta t = 0.0001$ ,  $\Delta x = 1/256$ : — trailing,  $\cdots$  leading. Results provided by Pan: - - - trailing, - · - leading. Vertical position (left), vertical velocity (right). The interval during which the repulsion force takes finite values is indicated near the abscissa.

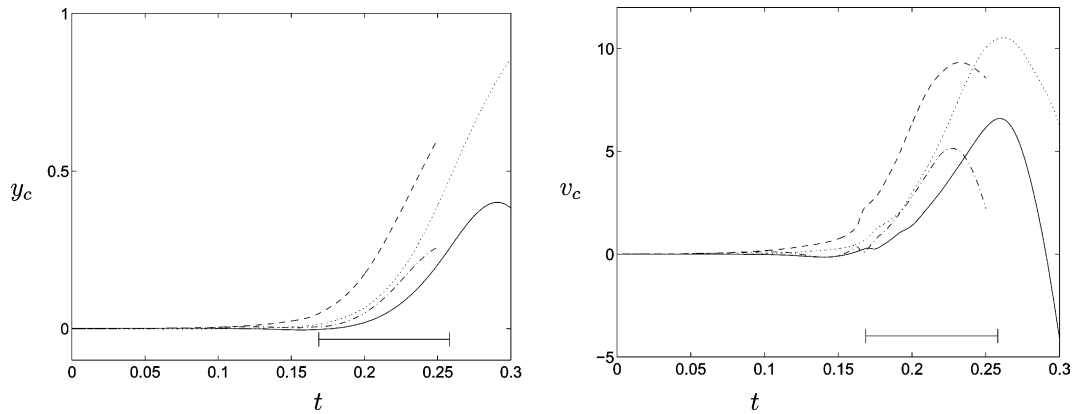


Fig. 7. Drafting–kissing–tumbling of two sedimenting discs with density  $\rho_p/\rho_f = 1.5$  which are initially aligned vertically. Results obtained with the present method,  $\Delta t = 0.0001$ ,  $\Delta x = 1/256$ : — trailing,  $\cdots$  leading. Results provided by Pan: - - - trailing, - · - leading. Horizontal position (left), horizontal velocity (right).

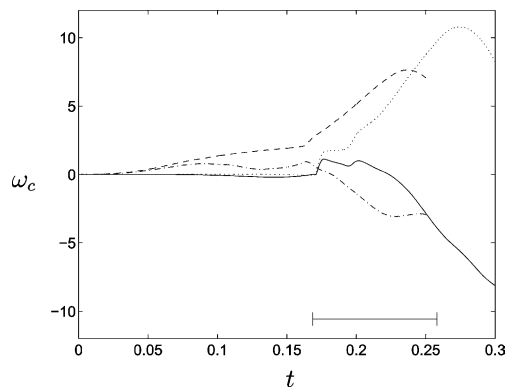


Fig. 8. Rotational velocity vs. time during the interaction of two sedimenting discs with density  $\rho_p/\rho_f = 1.5$  which are initially aligned vertically. Results obtained with the present method,  $\Delta t = 0.0001$ ,  $\Delta x = 1/256$ : — trailing,  $\cdots$  leading; results provided by Pan: - - - trailing, - · - leading.

Particularly, a much more pronounced lateral motion is manifest in the data-set of Pan. In our computations, a lateral motion of the particle during “drafting” is only observed if the initial position is chosen non-symmetric w.r.t. the grid since our spatial scheme fully preserves the symmetry and perturbations due to finite-precision arithmetic do not grow fast enough for these short times. With the present small lateral offset of the initial particle position, lateral motion sets in quickly, albeit to a much lesser extent than exhibited by the results provided by Pan. We believe that the anisotropic triangular grid used therein is responsible for the larger lateral motion as well as for a higher angular velocity (cf. related discussion in reference [8]). During “kissing” and “tumbling”, however, the lateral motion and rotation obtained by our method show a similar behavior as Pan’s results. It should be noted that our results for these later stages are sensitive to the choice of the initial horizontal offset.

### 5.2.2. Pure wake interaction

Two particles with a vertical and horizontal offset are released at  $t = 0$ . The trailing particle has a higher density and therefore passes the leading particle, subjecting it to perturbations in its wake. The computation

is stopped before the heavier particle reaches the bottom boundary of the computational domain. There are two reasons for discussing this test case:

- No direct particle–particle interactions are observed. Therefore, no numerical collision model is needed, making this case attractive as a possible future “benchmark” for testing the basic fluid–solid interaction method.
- Since the angular motion of the particles is non-negligible here, we can gauge the importance of the representation of the rate-of-change term  $\mathcal{J}$  (cf. Eq. (13b)). Specifically, we can deduce that using the approximate formulation given in Eq. (15) is an acceptable simplification.

The physical parameters of the problem are the following:

- domain size  $\Omega = [0, 10] \times [-1, 1]$ ;
- disc radius  $r_c^{(1)} = r_c^{(2)} = 0.1$ ;
- initial location of the discs  $\mathbf{x}_c^{(1)}(t=0) = (0.8, -0.13)$ ,  $\mathbf{x}_c^{(2)}(t=0) = (1.2, +0.13)$ ;
- density ratio  $\rho_p^{(1)}/\rho_f = 1.5$ ,  $\rho_p^{(2)}/\rho_f = 1.25$ ;
- fluid viscosity  $\nu = 0.0008$ ;
- gravitational acceleration  $\mathbf{g} = (9.81, 0)$ .

This yields maximum particle Reynolds numbers of 280 and 230, respectively. The numerical parameters are set to the following values:

- mesh width  $h = 1/200$ , i.e.  $D/h = 40$ ;
- time step  $\Delta t = 0.001$ , which leads to a maximum  $CFL$  number around 0.5.

The final time shown below is  $t_{\text{fin}} = 8.629$ , corresponding to the center of the heavy particle being located at  $2D$  above the bottom boundary.

Fig. 9 shows the trajectories of the two particles and Fig. 10 successive snapshots of the vorticity field. It can be observed that the heavier particle follows a slightly undulating path due to the oscillating lift force induced by its own vortex shedding. The deviation of the lighter particle’s path from a vertical one is more pronounced, partially due to the interaction with the preceding vortices. The time-evolution of particle positions and translational velocities is given in Figs. 11 and 12. It is noteworthy that the heavy particle’s vertical velocity reaches its maximum value and then slightly decelerates when vortex shedding has reached a periodic state.

Fig. 13 shows the particles’ angular position and velocity; Fig. 14 does the same for the results obtained with the approximate formulation for the angular momentum balance given in Eq. (15). It can be seen that

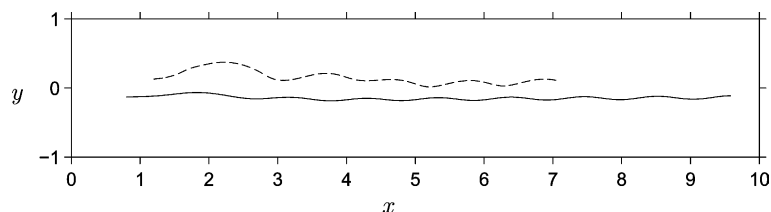


Fig. 9. Wake interaction of two sedimenting particles with density  $\rho_p^{(1)}/\rho_f = 1.5$ ,  $\rho_p^{(2)}/\rho_f = 1.25$  and initial vertical and lateral offset. The gravity acts in the positive  $x$ -direction. Results obtained with  $\Delta t = 0.001$ ,  $h = 1/200$ . The graph shows the particle trajectories with the line styles corresponding to: — heavy particle, --- light particle.



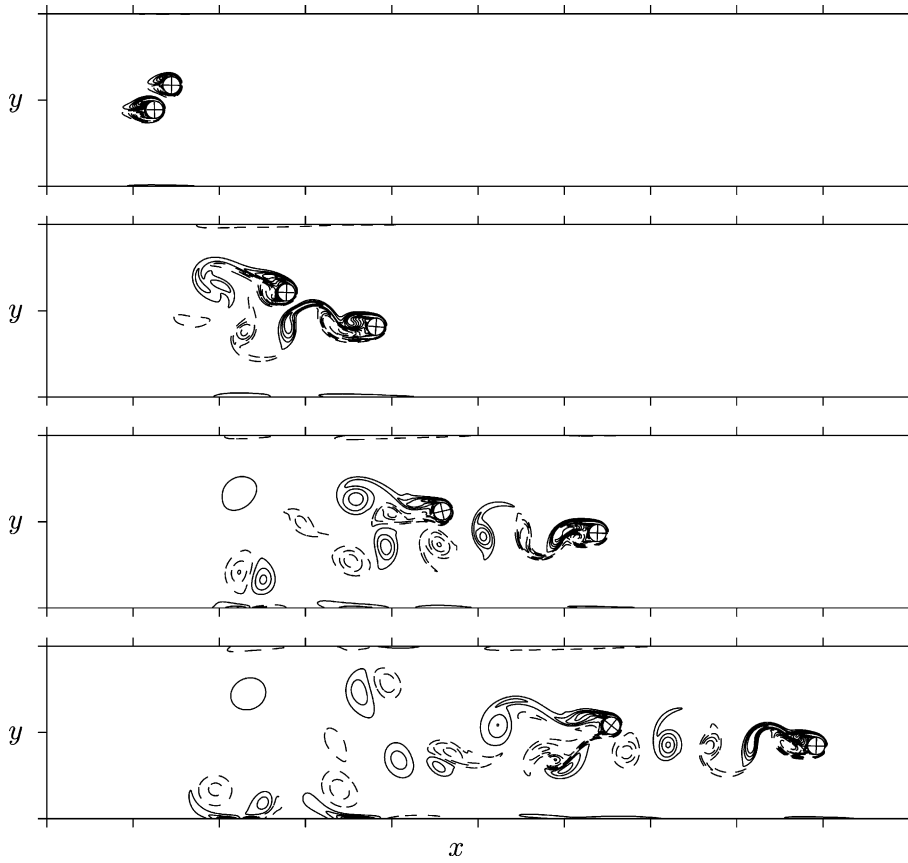


Fig. 10. Wake interaction case of Fig. 9. Instantaneous contours of vorticity (values at  $-30:4.6:30$ , negative values corresponding to dashed lines) and particle positions at times  $t = 0.8$ ,  $t = 3.2$ ,  $t = 5.6$ ,  $t = 8.0$  (from top to bottom) are shown. The crosses inside the circles indicate the angular position of the particles.

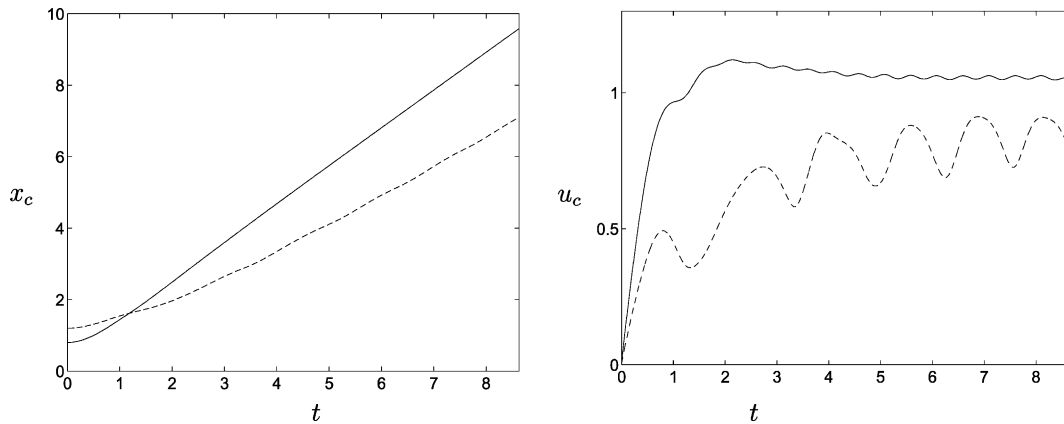


Fig. 11. Wake interaction case of Fig. 9. The graphs show: vertical particle positions (left), vertical particle velocities (right).

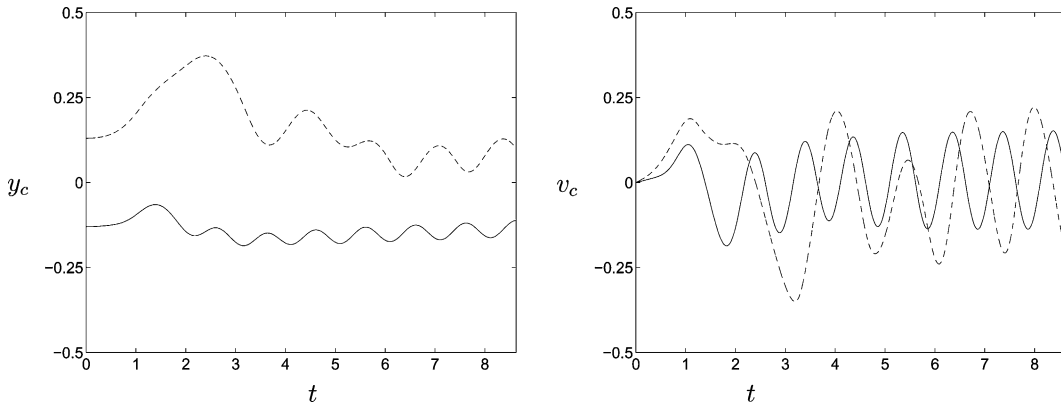


Fig. 12. Wake interaction case of Fig. 9. The graphs show: horizontal particle positions (left), horizontal particle velocities (right).

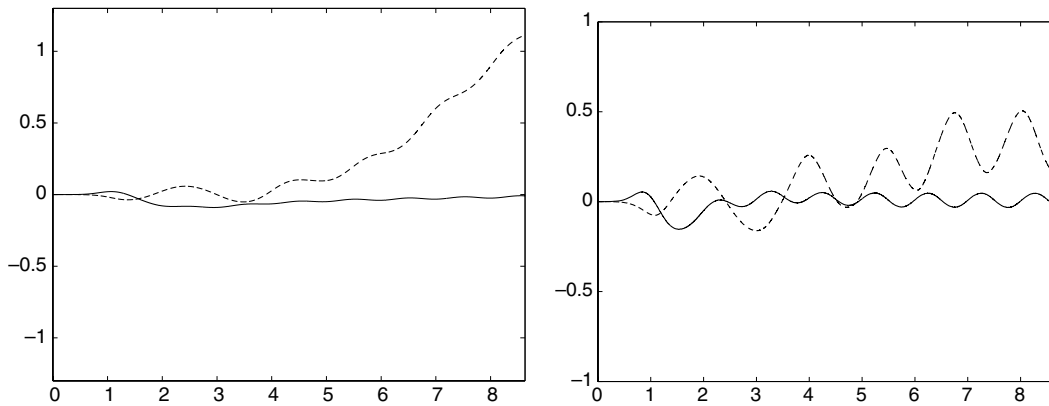


Fig. 13. Wake interaction case of Fig. 9. The graphs show: angular particle positions (left), angular particle velocities (right).

both variants yield qualitatively very similar results. The effect of the simplification is an increase of the amplitude of the oscillations of angular velocity. The root-mean-square value of the difference amounts to approximately 13% (18%) of the maximum angular velocity for the heavy (light) particle. At the same time, the particle trajectories coincide to within  $0.08D$  and  $0.54D$  for the heavy and light particle, respectively. As a conclusion we consider it acceptable to simplify the particles' angular momentum balance by using Eq. (15) in the subsequent three-dimensional cases.

### 5.3. Motion of spherical particles

Here we present simulations of the motion of three-dimensional spherically shaped particles. In all cases the flow-field and particle positions are treated as triply-periodic. Again, initially the fluid and the particles are at rest. In the following the particle-related quantities will be normalized with the reference values  $u_{\text{ref}} = \sqrt{|\mathbf{g}|D}$ ,  $t_{\text{ref}} = \sqrt{D/|\mathbf{g}|}$ ,  $l_{\text{ref}} = D$  for velocity, time and length, respectively.

#### 5.3.1. A single sedimenting sphere

We consider a single sphere which is released at  $t = 0$ . The parameters are chosen in order to match cases 1, 2, 4 of the experiment of Mordant and Pinton [34], where the motion of spherical beads in water was

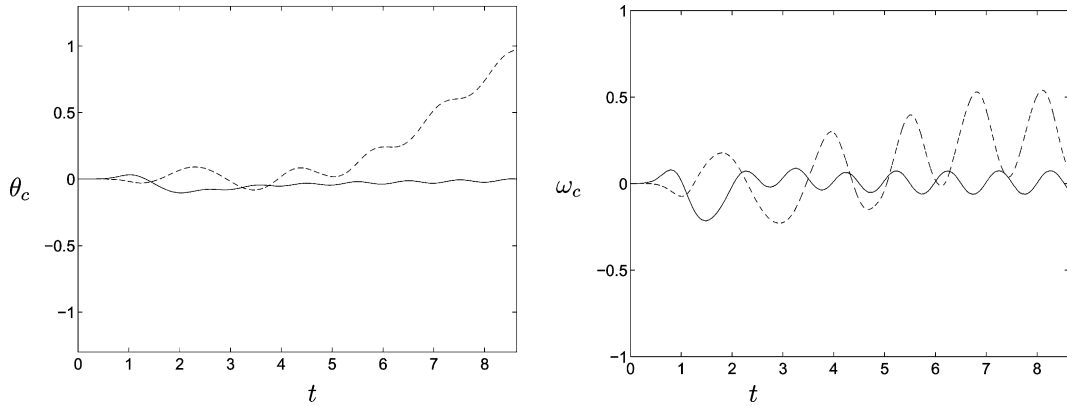


Fig. 14. The same as Fig. 13, but the results were obtained by using the approximation of full rigidity (Eq. (15)) for determining the rate-of-change term of angular particle momentum.

investigated, while their material and diameter were varied from case to case. This case has also been considered as a reference for the computations in [22]. The experiment takes place in a large container, justifying the use of periodic conditions in the simulation. We have selected the following parameters by similarity with the experiment, keeping the values for the density ratio, Froude number and particle Reynolds number constant:

- domain size  $\Omega = [0, 1.25] \times [0, 1.25] \times [0, L_z]$ ;
- particle radius  $r_c = 1/12$ ;
- initial particle location  $\mathbf{x}_c(t=0) = (0.625, 0.625, 9.5)$ ;
- gravitation vector  $\mathbf{g} = (0, 0, -9.81)$ ;
- and:

Case	1	2	4
Density ratio $\rho_p/\rho_f$	2.56	2.56	7.71
Domain length $L_z$	10	10	15
Fluid viscosity $\nu$	0.005416368	0.00104238	0.00267626

The values for the numerical parameters are:

- mesh width  $h = 1/76.8$ , i.e.  $D/h = 12.8$ ;
- time step  $\Delta t = 0.0025$ , i.e. yielding a maximum *CFL* number of 0.3, 0.75, 0.5, respectively.

Figs. 15–17 show the vertical velocity as a function of the elapsed time. The computational results are shown for times before the particle motion in the periodic domain is affected by the remnants of its own wake. A very good agreement with the experimental measurements can be observed in all three cases. Table 3 shows the terminal value of the Reynolds number whose maximum error is below 2% (case 2). Finally, we have reported the variation of the two horizontal velocity components in Fig. 18. The lateral motion is negligible in the low-Reynolds number case 1 due to the absence of asymmetric vortex shedding. In the other two cases vortex shedding induces horizontal velocities two orders of magnitude smaller than the vertical velocity.

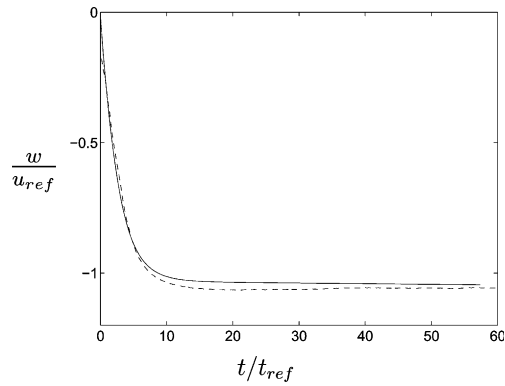


Fig. 15. Sedimentation of a single sphere; case 1 of reference [34]. Vertical velocity: — present, --- experimental data.

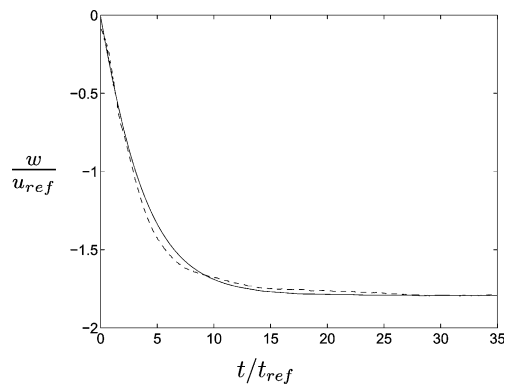


Fig. 16. Sedimentation of a single sphere; case 2 of reference [34]. Vertical velocity: — present, --- experimental data.

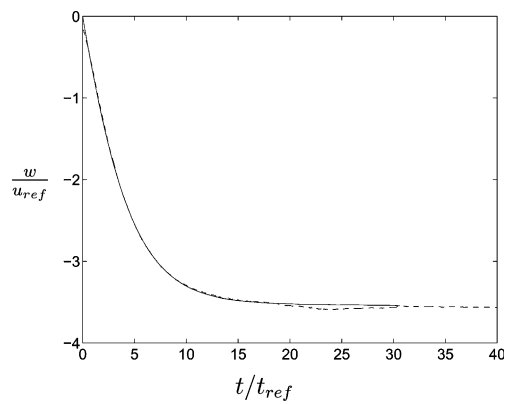


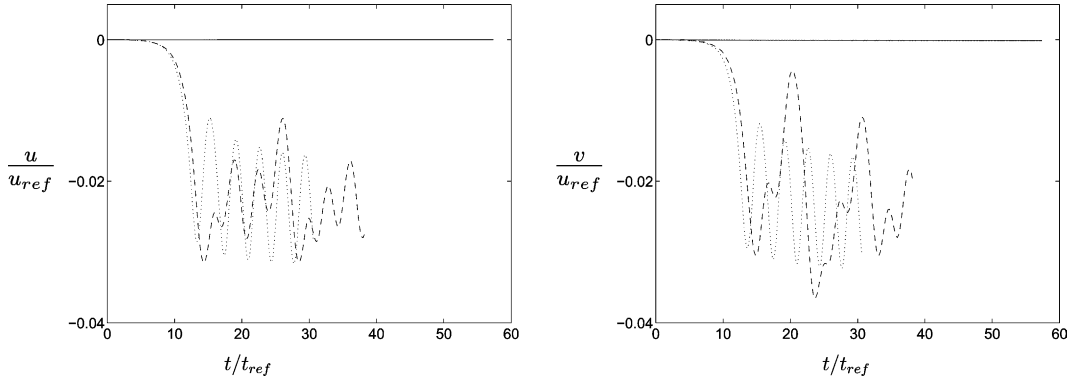
Fig. 17. Sedimentation of a single sphere; case 4 of reference [34]. Vertical velocity: — present, --- experimental data.

The importance of this test case should be underlined: it confirms – for a considerable range of Reynolds numbers – the present method’s ability to reproduce the dynamic behavior of a three-dimensional, suspended particle under the action of gravity, using reliable experimental data as a reference.

Table 3

Terminal particle Reynolds number  $Re_D$  in the case of a single sedimenting sphere, compared to the experiment of reference [34]

Case	1	2	4
Present	41.12	366.69	282.45
Experiment	41.17	362.70	280.42

Fig. 18. Sedimentation of a single sphere. Horizontal velocities  $u$  (left) and  $v$  (right). — case 1, --- case 2,  $\cdots$  case 4.

### 5.3.2. Many-particle systems

Here we consider the collective behavior of a number of identical particles under the action of gravity. The physical parameters are:

- particle radius  $r_c = 1/12$ ;
- density ratio  $\rho_p/\rho_f = 2.56$
- gravitational acceleration  $\mathbf{g} = (0, 0, -9.81)$
- fluid viscosity  $\nu = 0.001$

which corresponds to a terminal Reynolds number of approximately 400. The sedimentation process of many-particle systems in periodic boxes has been simulated in reference [4] for very low Reynolds numbers and in reference [6] for similar values of the Reynolds number.

The values for the numerical parameters are:

- mesh width  $h = 1/76.8$ , i.e.  $D/h = 12.8$ ;
- time step  $\Delta t = 0.002$ , i.e. yielding a maximum  $CFL$  number of approximately 0.5 after the initial transient.

We have studied three different configurations with 1, 63 and 1000 particles and different domain sizes. All relevant definitions are given in Table 4. The initial particle locations consist of uniform and symmetric arrays (sizes indicated in the table) with a small perturbation of the order of a few percent of the radius in order to speed up the transient. No collision model was used and the simulations were stopped when unphysical overlapping of particle domains was detected.

Fig. 19 shows the time-evolution of the average vertical particle velocity,  $\bar{w}_c = \sum_{i=1}^{N_p} w_c^{(i)} / N_p$ . In both many-particle cases this quantity initially reaches very high values before levelling off to values which

Table 4

Definitions for the three different configurations used in triply-periodic many-particle simulations in Section 5.3.2

Case		1	2	3
No. of particles	$N_p$	1	63	1000
Initial locations		(irrelevant)	$3 \times 3 \times 7$ array	$10 \times 10 \times 10$ array
Domain size	$\Omega$	$[0, 1.6]^2 \times [0, 5]$	$[0, 1.6]^2 \times [0, 5]$	$[0, 6.6]^3$
Volume fraction of solids	$\epsilon_p$	0.000175	0.011	0.0082
Mass loading ratio of solids	$\phi_p$	0.000447	0.0285	0.0211

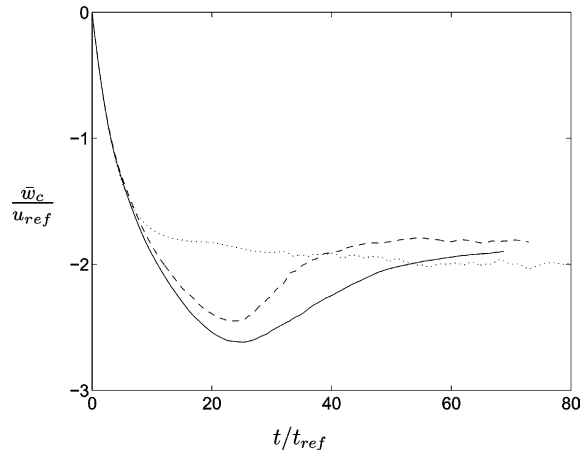


Fig. 19. Sedimentation of an array of  $N_p$  identical spheres with density ratio  $\rho_p/\rho_f = 2.56$  and terminal Reynolds number approximately 400. Mean vertical particle velocity vs. time for:  $\cdots$  case 1 ( $N_p = 1$ ),  $---$  case 2 ( $N_p = 63$ ),  $—$  case 3 ( $N_p = 1000$ ).

are similar to the single-particle case 1. This transient behavior is due to the particles' initial vertical alignment which leads to a relatively low drag because of wake-sheltering. As soon as the configuration is perturbed through the onset of asymmetric vortex-shedding the drag increases again leading to the observed reduction of the settling velocity.

In Fig. 20 we have plotted the time-evolution of the average distance to the nearest particle,  $\bar{d}_{\min} = \sum_{i=1}^{N_p} \min_j (|\mathbf{x}_c^{(i)} - \mathbf{x}_c^{(j)}|)$ , which is an indicator for the re-organization of the relative particle positions. It can be observed that  $\bar{d}_{\min}$  gradually decreases in cases 2 and 3, showing that indeed there is a tendency for particles to attract each other.

Finally, Figs. 21 and 22 show visualizations of the instantaneous particle positions and the flow field in case 3 at  $t/t_{\text{ref}} = 64.445$ . It is evident that the initially uniform and symmetric particle configuration has broken up and given way to a seemingly disordered state by this time. The vortex tubes reaching from particle to particle and the entangled streamlines show how neighboring particles are indirectly interacting by way of the fluid.

#### 5.4. A note on efficiency

The main work in the pure fluid part of our method stems from the multi-grid solution of the Poisson problem (12f) and the factorized solution of the Helmholtz problems (12e). Therefore, the overall operation count for the fluid scales as  $\mathcal{O}(N^3)$ , where  $N$  is the number of Eulerian grid nodes in one spatial dimension.

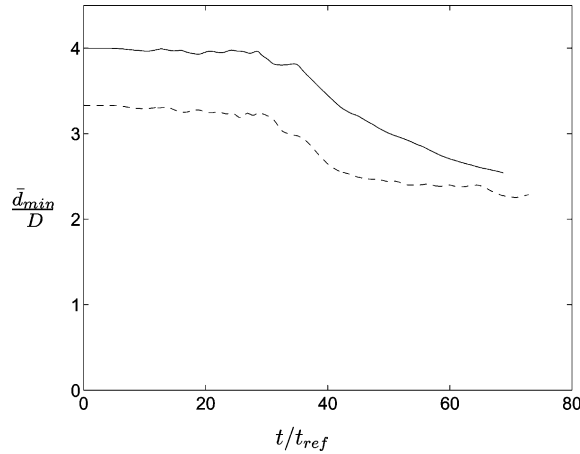


Fig. 20. Sedimentation of an array of  $n$  identical spheres with density ratio  $\rho_p/\rho_f = 2.56$  and terminal Reynolds number approximately 400. Mean distance to the nearest particle vs. time for: --- case 2 ( $N_p = 63$ ), — case 3 ( $N_p = 1000$ ).

On the other hand, the solution of the Newton equations (13) for  $N_p$  particles requires simply  $\mathcal{O}(N_p)$  operations. Finally, the fluid–solid interaction in Eqs. (12b)–(12d) is performed in  $\mathcal{O}(N_p N_L)$  operations. Since the number of Lagrangian force points  $N_L$  is chosen such that each one controls a volume corresponding to a grid cell we have approximately from (A.5) that  $N_L \sim (D/h)^2$ . Introducing a characteristic macroscopic length scale  $L = Nh$ , we arrive at the following count for the fluid–solid coupling:  $\mathcal{O}(N_p (D/L)^2 N^2)$ . This

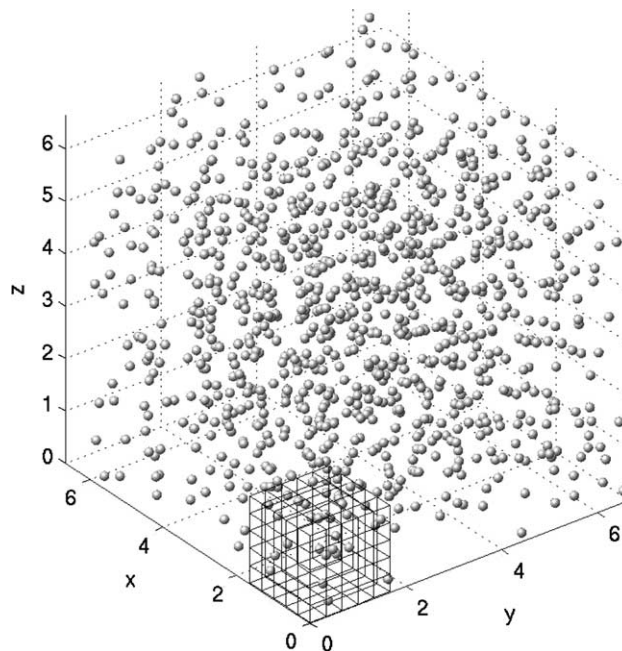


Fig. 21. Instantaneous particle positions in the sedimentation case 3 ( $N_p = 1000$ ) at  $t/t_{ref} = 64.445$ . The small wire-frame cube indicates the sub-volume visualized in Fig. 22.

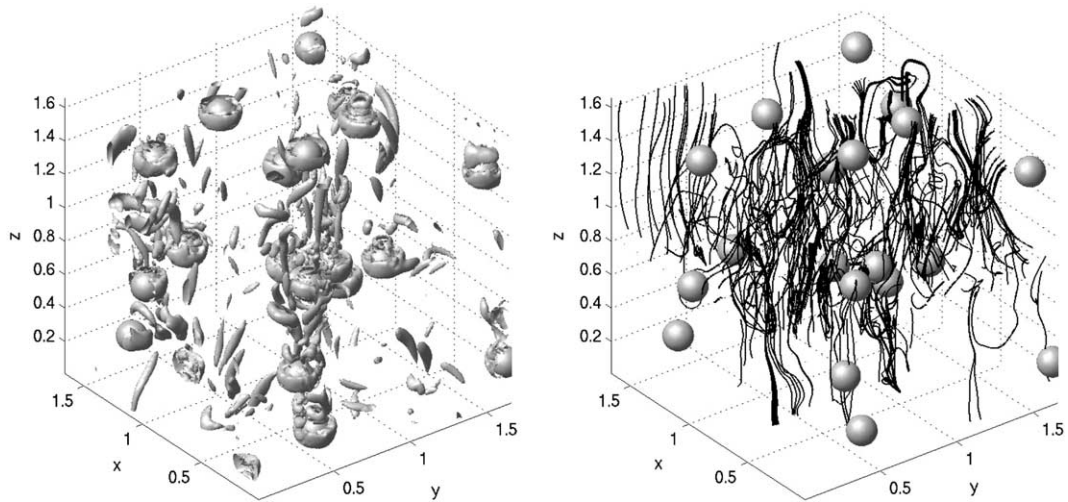


Fig. 22. Visualization of the instantaneous flow field and particle positions in a sub-volume indicated in Fig. 21 of the sedimentation case 3 ( $N_p = 1000$ ) at  $t/t_{ref} = 64.445$ . The left graph shows iso-surfaces of positive values of the Laplacian of pressure, indicating vortex cores. The right graph shows streamlines released from the horizontal mid-plane.

Table 5

Execution time (per full time step),  $t_{exec}$ , of the present scheme on an IBM p655 cluster with Power 4, 1.1 GHz CPUs and Colony switch, 64 bit arithmetic, performing 6–7 multi-grid iterations for each Poisson problem

$N_x \times N_y \times N_z$	$N_p$	$N_L$	nproc	$t_{exec}$ [s]
$512 \times 512 \times 512$	1000	515	64	115.0
$512 \times 512 \times 1024$	1000	515	128	144.9
$512 \times 512 \times 1024$	2000	515	128	147.4

The parameters are: grid size  $N_x, N_y, N_z$ , number of particles  $N_p$ , number of Lagrangian force points per particle  $N_L$  and number of processors nproc.

shows that even for tightly packed particles (i.e.  $N_p = (L/D)^3$ ) the work needed for treating the pure fluid part of the code asymptotically outweighs the remaining contributions (since  $L/D < N$ ).

In order to deal with large-scale problems the algorithm was implemented for multi-processor machines with distributed-memory. Classical domain-distribution was used for the fluid part and a master-slave technique was employed for the particle-related operations [35]. Table 5 shows some execution times per time step of “production size” cases. For the largest case involving  $512^2 \times 1024$  grid nodes and 128 processors, it can be seen that increasing the number of particles from 1000 to 2000 increases the execution time by less than 2%.

## 6. Conclusion

We have presented an improved immersed-boundary method with a direct formulation of the fluid–solid interaction force. The regularized delta function of Peskin [23] is used for the association between arbitrary Lagrangian and discrete Eulerian positions. Thereby, the hydrodynamic forces acting upon the particles are



free from significant oscillations, allowing for smooth motion of the particles. On the other hand, the direct (not feed-back) character of the forcing scheme avoids additional restrictions of the time-step.

The current method was implemented in a finite-difference and fractional-step context. The fluid equations are weakly coupled to the Newton equations for the rigid-body motion of the particles which imposes a lower limit for the density ratio between particles and fluid of approximately 1.2 for stable integration.

The new scheme was applied to Taylor–Green flow, flow around fixed and oscillating cylinders as well as sedimentation problems in two and three space dimensions. By comparison of our present results with reference values from experiments and independent numerical simulations we have demonstrated the high accuracy of the method. Furthermore, our simulations of many-particle systems in truly three-dimensional domains using multi-processor machines show that the study of large-scale configurations is feasible with the current approach.

## Acknowledgments

This work was supported by the Spanish Ministry of Education and Science under the Ramón y Cajal program (contract DPI-2002-040550-C07-04) and through grant DPI-2002-1314-C07-04. Part of the work was done while the author was visiting the Department of Aeronautics and Astronautics at the University of Kyoto, Japan, with the aid of a grant from the Japanese Society for the Promotion of Science. Additional computing time was provided by the Potsdam Institute for Climate Impact Research, Germany.

## Appendix A. Distribution of Lagrangian force points and associated volumes

In practice we want each force point to control a volume which is equivalent to a finite volume of the Eulerian grid, i.e.  $\Delta V_l \approx h^n$ , where  $n$  is the number of space-dimensions. We have verified that further increasing the number of force points  $N_L$  does not significantly improve the solution. Therefore, in all present simulations  $N_L$  was determined from Eqs. (A.3) and (A.5).

### A.1. Circular particles

We define a number of  $N_L$  elements around the circumference of a circular solid object, as shown in Fig. 23. The elements are equi-partitioned sectors of an annulus with inner and outer radii  $r_1$ ,  $r_2$ , respectively. The actual particle radius  $r_c$  is located at the midpoint of these two radii  $r_c = (r_2 + r_1)/2$ . Furthermore, we take the radial width of an element to be equal to the mesh size  $h$ ,  $h = r_2 - r_1$ . The arc-length, measured at radius  $r_c$ , is given by  $\delta s = 2\pi r_c/N_L$ . It follows then that

$$r_1 = r_c - \frac{h}{2}, \quad r_2 = r_c + \frac{h}{2}, \quad (\text{A.1})$$

which gives for the surface of an element  $\Delta V_l$ :

$$\Delta V_l = \frac{2\pi r_c h}{N_L}. \quad (\text{A.2})$$

We associate a Lagrangian force point to each of the above elements and locate it equidistantly on the actual circumference of the particle (i.e. in the center of an element).

Requiring that  $\Delta V_l \approx h^2$  leads to the following condition for the number of force points:

$$N_L \approx 2\pi \frac{r_c}{h}. \quad (\text{A.3})$$

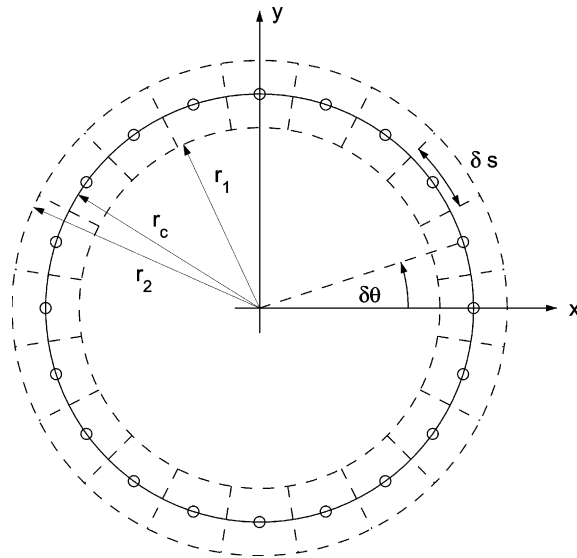


Fig. 23. Definitions for a circular particle.  $r_c$  is the actual particle radius and small circular symbols indicate the (equidistant) locations of Lagrangian force points; the dashed lines show the extent of the volumes associated with each force point.

## A.2. Spherical particles

### A.2.1. Force point distribution

The even distribution of an arbitrary number of points on the surface of a sphere is an unsolved problem in geometry [36]. In fact the very definition of “even” is not evident. In practice two methods appear feasible for our case:

- (1) Start with one of the three triangular-faced regular polyhedra (tetrahedron, octahedron, icosahedron) whose vertices lie on the surface of a sphere. Among these Platonic solids, the icosahedron has the highest number of rotational symmetries and therefore leads to the most “even” distribution of points. In each refinement step, “pull-up” the centroid of each edge to the sphere’s surface and thereby subdivide each of its previous faces into four new triangular faces. The final number of vertices after  $m$  such refinement steps is  $N_L = n_v + \sum_{i=1}^m n_e 4^{i-1}$ , where  $n_v$ ,  $n_e$  are the number of initial vertices and edges, respectively. Obviously the values of  $N_L$  which can be obtained in this fashion are very sparsely distributed. For values outside this set, one needs to resort to the following method.
- (2) Define “even” as the configuration of points which minimizes the total repulsive energy in a system of charged particles. For a given value of  $N_L$ , run a simulation of the motion of point-particles confined to the surface of a sphere. From some initial state, using a mutual repulsive force which is proportional to the inverse of the square of the inter-particle distance, an equilibrium configuration can be obtained iteratively. Several runs with different initial conditions might be necessary in order to find a global energy minimum. An example for  $N_L = 515$  is shown in Fig. 24.

### A.2.2. Definition of forcing volumes

A spherical shell between the radii  $r_1 = r_c - h/2$  and  $r_2 = r_c + h/2$  shall be forced (cf. Fig. 24). Therefore, we associate the following partial volume with each force point:

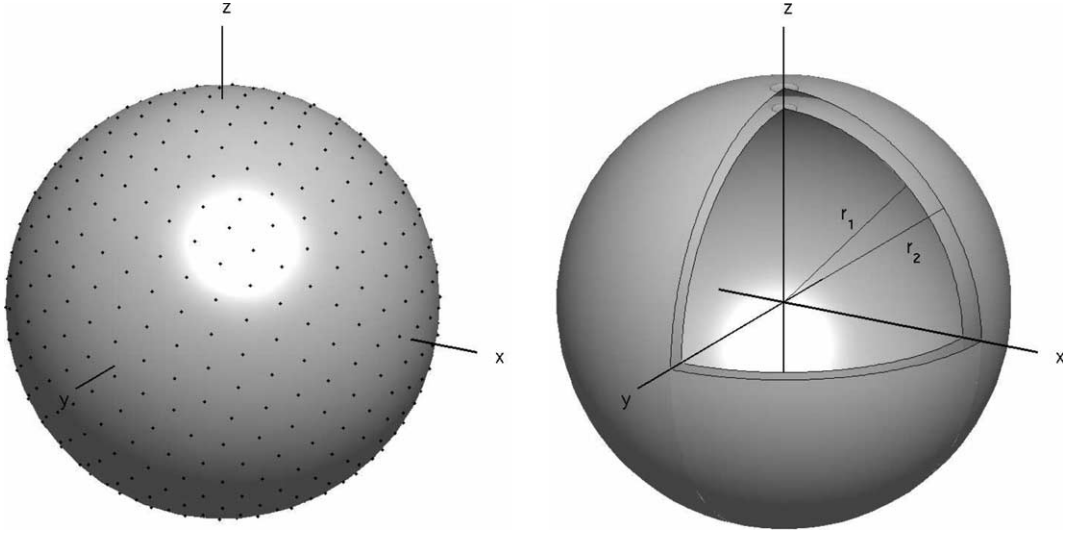


Fig. 24. Definitions for a spherical particle. In the graph on the left an iteratively obtained distribution of the Lagrangian force points for the case  $N_L = 515$  is shown. The right graph shows a cut-away view of the thin shell between radii  $r_1$  and  $r_2$  where forcing is applied.

$$\Delta V_l = \frac{\pi h}{3N_L} (12r_c^2 + h^2). \quad (\text{A.4})$$

Requiring that  $\Delta V_l \approx h^3$  leads to the following condition for the number of force points:

$$N_L \approx \frac{\pi}{3} \left( 12 \frac{r_c^2}{h^2} + 1 \right). \quad (\text{A.5})$$

## Appendix B. Evaluation of the hydrodynamic forces acting upon particles

Let us write Newton's equations for the motion of a single rigid particle, viz.

$$\rho_p V_c \dot{\mathbf{u}}_c = \rho_f \oint_{\partial S} \boldsymbol{\tau} \cdot \mathbf{n} d\sigma + (\rho_p - \rho_f) V_c \mathbf{g}, \quad (\text{B.1a})$$

$$I_c \dot{\boldsymbol{\omega}}_c = \rho_f \oint_{\partial S} \mathbf{r} \times (\boldsymbol{\tau} \cdot \mathbf{n}) d\sigma, \quad (\text{B.1b})$$

where  $\boldsymbol{\tau} = -Ip + v(\nabla \mathbf{u} + \nabla \mathbf{u}^T)$  is the hydrodynamic stress tensor,  $\mathbf{n}$  the outward-pointing normal vector on the fluid–solid interface  $\partial S$  and  $\mathbf{r} = \mathbf{x} - \mathbf{x}_c$ . Cauchy's principle states for the hydrodynamic force and torque terms [37, p. 100]:

$$\oint_{\partial S} \boldsymbol{\tau} \cdot \mathbf{n} d\sigma = - \int_S \mathbf{f} d\mathbf{x} + \frac{d}{dt} \int_S \mathbf{u} d\mathbf{x}, \quad (\text{B.2a})$$

$$\oint_{\partial S} \mathbf{r} \times (\boldsymbol{\tau} \cdot \mathbf{n}) d\sigma = - \int_S \mathbf{r} \times \mathbf{f} d\mathbf{x} + \frac{d}{dt} \int_S (\mathbf{r} \times \mathbf{u}) d\mathbf{x}. \quad (\text{B.2b})$$

The first term on the r.h.s. of both equations in (B.2) is simply the negative of the sum of the fluid–solid coupling force/torque defined in Section 3.2. Using the equalities (11) these can be efficiently evaluated as sums over the Lagrangian force points. Concerning the rate-of-change term in the force relation (B.2a) it can be shown that the following expression holds for an incompressible fluid which satisfies a rigid-body motion on the interface  $\partial S$  [17]:

$$\frac{d}{dt} \int_S \mathbf{u} \, d\mathbf{x} = V_c \dot{\mathbf{u}}_c \quad (\text{B.3})$$

irrespective of the actual type of motion inside the volume  $S$ . Conversely, the analogous relation for the torque only holds in the case of rigid-body motion throughout the volume  $S$ :

$$\mathbf{u}(\mathbf{x}) = \mathbf{u}_c + \boldsymbol{\omega}_c \times \mathbf{r}(\mathbf{x}) \quad \mathbf{x} \in S : \quad \frac{d}{dt} \int_S \mathbf{r} \times \mathbf{u} \, d\mathbf{x} = \frac{I_c}{\rho_p} \dot{\boldsymbol{\omega}}_c. \quad (\text{B.4})$$

In our case, i.e. when the inner part of the solid particles is not forced, no simplification could be found and the rate-of-change of the integral of the torque must be evaluated numerically. Finally, collecting all terms yields the form of Newton’s equations (13) given in the main text.

## References

- [1] S. Sundaresan, Modeling the hydrodynamics of multiphase flow reactors: current status and challenges, *AIChE J.* 46 (6) (2000) 1102–1105.
- [2] P. Moin, K. Mahesh, Direct numerical simulation: a tool in turbulence research, *Ann. Rev. Fluid Mech.* 30 (1998) 539–578.
- [3] H. Hu, N. Patankar, N. Zhu, Direct numerical simulation of fluid–solid systems using the arbitrary Lagrangian Eulerian technique, *J. Comput. Phys.* 169 (2001) 427–462.
- [4] K. Höfler, S. Schwarzer, Navier–Stokes simulation with constraint forces: finite-difference method for particle-laden flows and complex geometries, *Phys. Rev. E* 61 (6) (2000) 7146–7160.
- [5] J. Kim, D. Kim, H. Choi, An immersed-boundary finite-volume method for simulations of flow in complex geometries, *J. Comput. Phys.* 171 (2001) 132–150.
- [6] T. Kajishima, S. Takiguchi, Interaction between particle clusters and particle-induced turbulence, *Int. J. Heat Fluid Flow* 23 (2002) 639–646.
- [7] R. Glowinski, T. Pan, T. Hesla, D. Joseph, J. Périaux, A fictitious domain approach to the direct numerical simulation of incompressible viscous flow past moving rigid bodies: application to particulate flow, *J. Comput. Phys.* 169 (2001) 363–426.
- [8] Z. Zhang, A. Prosperetti, A method for particle simulation, *J. Appl. Mech.* 70 (2003) 64–74.
- [9] Z.-G. Feng, E. Michaelides, The immersed boundary-lattice Boltzmann method for solving fluid–particles interaction problems, *J. Comput. Phys.* 195 (2) (2004) 602–628.
- [10] C. Peskin, Flow patterns around heart valves: a digital computer method for solving the equations of motion, Ph.D. thesis, Albert Einstein College of Medicine, 1972.
- [11] A. Fogelson, C. Peskin, A fast numerical method for solving the three-dimensional Stokes’ equations in the presence of suspended particles, *J. Comput. Phys.* 79 (1988) 50–69.
- [12] M.-C. Lai, C. Peskin, An immersed boundary method with formal second-order accuracy and reduced numerical viscosity, *J. Comput. Phys.* 160 (2000) 705–719.
- [13] E. Saiki, S. Biringen, Numerical simulation of a cylinder in uniform flow: application of a virtual boundary method, *J. Comput. Phys.* 123 (1996) 450–465.
- [14] C. Lee, Stability characteristics of the virtual boundary method in three-dimensional applications, *J. Comput. Phys.* 184 (2003) 559–591.
- [15] D. Goldstein, R. Handler, L. Sirovich, Modeling a no-slip boundary with an external force field, *J. Comput. Phys.* 105 (1993) 354–366.
- [16] E. Fadlun, R. Verzicco, P. Orlandi, J. Mohd-Yusof, Combined immersed-boundary finite-difference methods for three-dimensional complex flow simulations, *J. Comput. Phys.* 161 (2000) 35–60.
- [17] M. Uhlmann, First experiments with the simulation of particulate flows, Technical Report No. 1020, CIEMAT, Madrid, Spain, ISSN 1135-9420, 2003.
- [18] R. Glowinski, T.-W. Pan, T. Hesla, D. Joseph, A distributed Lagrange multiplier/fictitious domain method for particulate flows, *Int. J. Multiphase Flow* 25 (1999) 755–794.

- [19] T. Pan, D. Joseph, R. Bai, R. Glowinski, V. Sarin, Fluidization of 1204 spheres: simulation and experiment, *J. Fluid Mech.* 451 (2002) 169–191.
- [20] N. Patankar, P. Singh, D. Joseph, R. Glowinski, T.-W. Pan, A new formulation of the distributed Lagrange multiplier/fictitious domain method for particulate flows, *Int. J. Multiphase Flow* 26 (2000) 1509–1524.
- [21] N. Patankar, A formulation for fast computations of rigid particulate flows, *CTR Res. Briefs* (2001) 185–196.
- [22] N. Sharma, N. Patankar, A fast computation technique for the direct numerical simulation of rigid particulate flows, *J. Comput. Phys.*, in press, doi:10.1016/j.jcp.2004.11.012.
- [23] C. Peskin, The immersed boundary method, *Acta Numerica* 11 (2002) 1–39.
- [24] M. Uhlmann, New results on the simulation of particulate flows, Technical Report No. 1038, CIEMAT, Madrid, Spain, ISSN 1135-9420, 2004.
- [25] A. Roma, C. Peskin, M. Berger, An adaptive version of the immersed boundary method, *J. Comput. Phys.* 153 (1999) 509–534.
- [26] M. Rai, P. Moin, Direct simulation of turbulent flow using finite-difference schemes, *J. Comput. Phys.* 96 (1991) 15–53.
- [27] R. Verzicco, P. Orlandi, A finite-difference scheme for three-dimensional incompressible flows in cylindrical coordinates, *J. Comput. Phys.* 123 (1996) 402–414.
- [28] U. Schumann, R. Sweet, A direct method for the solution of Poisson's equation with Neumann boundary conditions on a staggered grid of arbitrary size, *J. Comput. Phys.* 20 (1976) 171–182.
- [29] C. Liu, X. Zheng, C. Sung, Preconditioned multigrid methods for unsteady incompressible flows, *J. Comput. Phys.* 139 (1998) 35–57.
- [30] M. Behr, D. Hastreiter, S. Mittal, T. Tezduyar, Incompressible flow past a circular cylinder: dependence of the computed flow field on the location of the lateral boundaries, *Comput. Methods Appl. Mech. Eng.* 123 (1995) 309–316.
- [31] M.N. Linnick, H.F. Fasel, A high-order immersed interface method for simulating unsteady incompressible flows on irregular domains, *J. Comput. Phys.* 204 (1) (2005) 157–192.
- [32] J. Park, K. Kwon, H. Choi, Numerical solutions of flow past a circular cylinder at Reynolds numbers up to 160, *KSME Int. J.* 12 (6) (1998) 1200–1205.
- [33] X.Y. Lu, C. Dalton, Calculation of the timing of vortex formation from an oscillating cylinder, *J. Fluids Structures* 10 (1996) 527–541.
- [34] N. Mordant, J.-F. Pinton, Velocity measurement of a settling sphere, *Eur. Phys. J. B* 18 (2000) 343–352.
- [35] M. Uhlmann, Simulation of particulate flows on multi-processor machines with distributed memory, CIEMAT Technical Report No. 1039, Madrid, Spain, ISSN 1135-9420, 2003.
- [36] E. Saff, A. Kuijlaars, Distributing many points on a sphere, *Math. Intelligencer* 19 (1) (1997) 5–11.
- [37] R. Aris, *Vectors, Tensors, and the Basic Equations of Fluid Mechanics*, Dover Science and Maths, 1962.